# CADMIUM JUMP FREQUENCIES IN $L1_2$ INTERMETALLIC COMPOUNDS

By

**XIA JIANG**

A thesis submitted in partial fulfillment of the
requirements for the degree of

MASTER OF SCIENCE IN PHYSICS

WASHINGTON STATE UNIVERSITY
Department of Physics and Astronomy

May 2008

To the Faculty of Washington State University:

The members of the Committee appointed to examine the thesis of XIA JIANG find it satisfactory and recommend that it be accepted.

_____
Chair

_____

_____

## ACKNOWLEDGMENTS

I am grateful to Prof. Gary S. Collins for introducing me into the field of nuclear condensed matter physics, for his guidance in the selection of research topics and the interpretation of experimental results, and for his patience in answering my many questions.

I would like to thank Prof. Matthew O. Zacate for his helpful comments on jump mechanisms.

My thanks go to John Bevington for his help with sample preparation and data processing, and for sharing his expertise on the instruments. I owe my thanks to Randal Newhouse for his kind help with experiments.

I would also like to thank Arriety Lowell, , Benjamin Norman and Justin Ann for the constructive discussions with them.

This work is supported in part by the National Science Foundation under grant DMR 05-04843 (Metals Program)

CADIMIUM JUPM FREQUENCIES IN $L1_2$

INTERMETALLIC COMPOUNDS

Abstract

by Xia Jiang, M.S.
Washington State University
May 2008

Chair: Gary S. Collins

Perturbed angular correlation spectroscopy was applied to study atomic movement in $L1_2$ type rare earth indides, gallides and aluminides. Nuclear relaxations were measured as a function of temperature and were related to the jump frequencies of $^{111}$In/Cd tracers by the XYZ model. Activation enthalpies were obtained by fitting jump frequencies to the Arrhenius temperature dependence. Measurements were made on opposing phase boundaries of the indide phases and the jump frequency was found to be highly dependent on the composition of the samples. Higher jump frequency and lower activation enthalpy were observed at the more In-rich phase boundary for the early rare earth indides and at the less In-rich phase boundary for the late rare earth indides. This reversal of behavior strongly suggests the existence of different diffusion mechanisms. The behavior of the late rare earth indides can be explained by a simple monovacancy diffusion mechanism. Three mechanisms are discussed in order to explain the behavior of the early rare earth indides, among which the six jump cycle mechanism is decided to be the most feasible one. With the assumption of this mechanism, the differences between activation enthalpies for the opposing phase boundaries are attributed to formation enthalpies of rare earth vacancies.

## TABLE OF CONTENTS

## LIST OF FIGURES

## LIST OF TABLES

# 1. Introduction

Diffusion in solids has traditionally been studied by using radioactive tracers and depth profiling techniques. More recently, it has also been studied on a microscopic level by such techniques as mechanical spectroscopy, nuclear magnetic relaxation and Mossbauer spectroscopy.[10] The latter methods usually measure a physical quantity that is sensitive to atomic movement in solids. In this work, Perturbed Angular Correlation (PAC) Spectroscopy was employed to study atomic movements.

PAC measures the electric field gradient (EFG) at a certain probe atom site. When probe atoms jump among lattice sites that possess different EFGs, nuclear relaxation is caused and PAC may be applied to measure the atomic jump frequency. This method was first applied to study diffusion in solids by Zacate, Favrot and Collins.[1] A review of the advantages and disadvantages of PAC method for diffusion study was given by Zacate et al.[1] and is summarized here. The advantages include: 1, PAC is sensitive to bulk diffusion and thus one need not worry about the effect of atom migration on irregular sites such as in lattice dislocations or grain boundaries. 2, PAC gives information that helps to identify the sublattice on which probes jump through the nuclear quadrupole interaction. 3, Measurements are made at thermal equilibrium. The disadvantages are: 1, PAC can only be applied to situations where the EFG changes for moving tracer atoms. 2, There is a limited number of PAC isotopes. 3, The jump frequency accessible to PAC is limited by inhomogeneous broadening and the quadrupole interaction frequency, being in the range 1-1000 MHz using the $^{111}$In/Cd probe.[2]

Diffusion in metals is a process of both theoretical interest and technical

importance, especially for their applications at high temperatures. Most studies in this area have concentrated on pure metals and dilute alloys, while relatively little information has been accumulated on intermetallics.[3] The present work focuses on diffusion in a type of binary intermetallic compounds which have the $L1_2$ structure (prototype: $AuCu_3$). These phases have the nominal composition $A_3B$ (throughout this paper, the majority atom will be designated by A and the minority atom B), and can be derived from the face-centered-cubic (fcc) structure (Fig. 1). A atoms occupy the face centers of the cubic unit cell, and are surrounded by 8 A-atoms and 4 B-atoms. On the other hand B atoms are surrounded exclusively by 12 A-atoms. For self diffusion, it is therefore quite natural to expect A atoms to migrate on their own sublattice, while the way B atoms diffuse is less clear.[10]

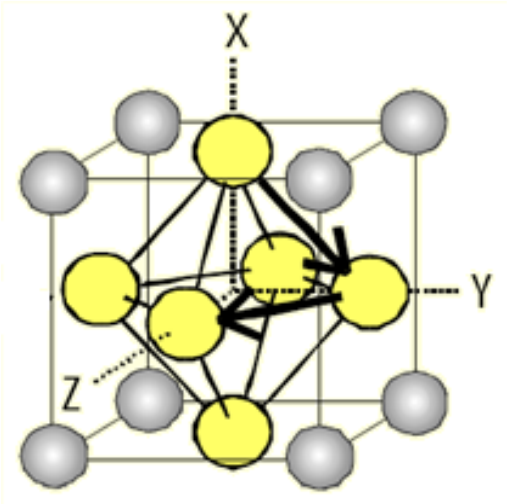


Fig. 1. Unit cell of $L1_2$ type $A_3B$ phase. The direction of the EFG at A-sites are marked by x, y and z.

In previous work of Collins and coworkers[1, 2, 4] PAC was applied to $L1_2$ type rare earth indides $RIn_3$ (R=La, Ce, Pr, Nd, Gd, Er, Y) and $LaSn_3$. All these phases appear in binary phase diagrams as "line" compounds, which means a compound having a definite composition, such as $A:B=75:25$. These compounds usually have phase fields narrower than 1 at.% and are commonly assumed to have properties independent of composition. However it has been found that jump frequencies in some of the indide and stanide phases mentioned above can vary significantly when measured at different phase boundary compositions. The present work extends jump frequency measurement to additional rare earth indides and also to rare earth gallides and aluminides in an effort to understand the systematics of jump frequencies, including activation enthalpies. Measurements were made for both more indium rich (designated as A) and less indium rich (designated as B) phase boundary compositions in order to shed light on the jump mechanism.

# 2. Theory

## 2.1 Perturbed angular correlation spectroscopy

Perturbed angular correlation spectroscopy is a time domain spectroscopy technique. It measures the coincidence rate of the emission of gamma rays from the probe nuclear decay, which gives information on the hyperfine interactions between the nuclear moments of probe atoms and the internal magnetic field and/or electric field gradient at the probe atom sites.

### 2.1.1 Spin alignment and unperturbed angular correlation of gamma-rays

In PAC spectroscopy, radioactive nuclides which emit two consecutive gamma-rays during their decay process are used as probes. The gamma rays are detected by two or more detectors and the coincidence rate is recorded as a function of time. Between the emissions of the two gamma-rays, the nuclides stay at on an intermediate energy level. The detection of the first gamma-ray amounts to a selection of preferred nuclear spin substates of the intermediate level, or in other words, a spin alignment with respect to the direction of the first gamma-ray is produced.[5] As a result the angular distribution of the second gamma-ray emission is no longer random, but correlated to the direction of the first gamma-ray (Fig. 2). The probability of detecting the second gamma-ray at an angle θ with respect to the first one is described by the angular correlation function

$$W(\theta) = 1 + \sum_{k\ even} A_k P_k(\cos\theta), \qquad (2.1)$$

in which $P_k$'s are even order Legendre polynomials and $A_k$'s describe the degree of anisotropy and are functions of the spin quantum numbers of the initial, intermediate and final levels of the decay.

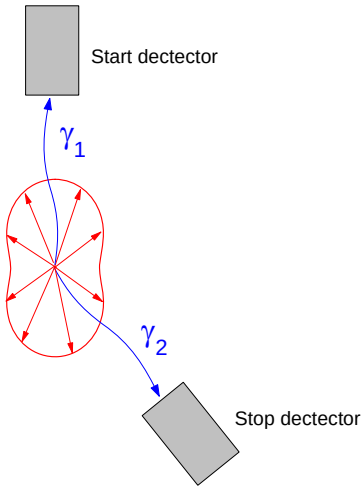


Fig. 2. Angular correlation of two gamma-ray emissions.

### 2.1.2 Spin precession and perturbed angular correlation of gamma-rays

An magnetic field or electric field gradient present at the site of the probe nuclei will cause hyperfine splitting of the energy level of the intermediate state. As a result the populations of the nuclear spin substates evolve with time and W(θ) becomes time-dependent. This is analogous to classical spin precession in an external field. For a random distribution of internal field orientations, Eq.(2.1) becomes[5]

$$W(\theta,t) = 1 + \sum_{k\ even} A_k G_k(t) P_k(\cos\theta). \qquad (2.2)$$

$G_k$(t) is called the *perturbation function* and its detailed form depends on the type of hyperfine interaction in question and the spin quantum numbers of the initial,

intermediate and final states of the decay.

### 2.1.3 Electric quadrupole interaction of $^{111}$In/$^{111}$Cd

One of the most important requirements of a PAC probe is that its intermediate level should have a long enough lifetime for the nuclide to complete a few precessions before it decays, so that useful information can be extracted. Some popular PAC probes include $^{111}$In/$^{111}$Cd, $^{181}$Hf/$^{181}$Ta and $^{100}$Pd/$^{100}$Rh.[6] In the present work $^{111}$In/$^{111}$Cd was used as probes in all the experiments. $^{111}$In has a mean lifetime of ~4.0 days and decays by electron capture into the second excited state of $^{111}$Cd, which then relaxes to its ground state by subsequent emissions of two gamma-rays with energies 171 keV and 245 keV (Fig. 3). The intermediate state (PAC level) has spin 5/2 and a mean lifetime of ~ 120 ns. The nuclear electric quadrupole moment of this state is $Q = 0.83(13)$ barn and the anisotropies are $A_2 = -0.18$ and $A_4 = -0.0015$.[6]

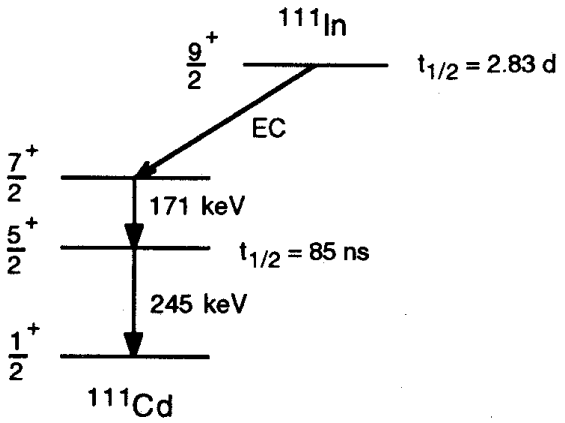


Fig. 3. Decay scheme of $^{111}$In

The form of the perturbation function depends on the symmetry of the electric field

gradient tensor. The EFG is a second-order tensor whose nine components are the second derivatives of the electric potential $V(\mathbf{r})$. When diagonalized by choosing a proper coordinate system the EFG can be fully described by three diagonal elements $V_{xx}$, $V_{yy}$, and $V_{zz}$ with the convention $|V_{zz}| \geq |V_{yy}| \geq |V_{xx}|$ . With the Poisson equation $V_{zz} + V_{yy} + V_{xx} = 0$, the EFG can be further reduced to two elements, namely $V_{zz}$ and $\eta$, where $\eta$ is the *EFG asymmetry parameter*, defined by:

$$\eta = (V_{xx} - V_{yy}) / V_{zz}. \tag{2.3}$$

Note that by definition $0 \leq \eta \leq 1$. It can be shown that for a site having a three-fold or higher axis of symmetry, $\eta = 0$. The magnitude of $V_{ij}$ can be estimated using a simple point charge model:

$$V_{ij} = (1 - \gamma_\infty) \sum_{\text{lattice ions}} \frac{q(\mathbf{r})(3x_i x_j - r^2 \delta_{ij})}{r^5}, \tag{2.4}$$

in which the summation gives the contribution from lattice ions and the factor $\gamma_\infty$ accounts for the polarization of the probe atoms' inner-shell electrons due to an external EFG. The term $(1 - \gamma_\infty)$ is of order -10 to -100 and thus determines the magnitude of the EFG.[6]

In case $\eta = 0$, the $I = 5/2$ intermediate state splits in such a way that the energy differences have the ratio $1:2:3$ (Fig. 4), giving rise to the hyperfine interaction frequencies with the same ratio.[5]

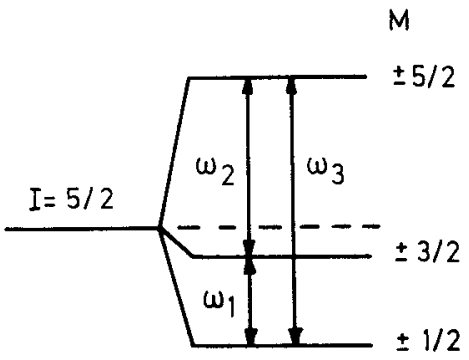


Fig. 4. Energy splitting of the $I = 5/2$ intermediate state.

Moreover, for axially symmetric case ($\eta = 0$) in a random polycrystalline sample, the perturbation function can be shown to have the following form:

$$G_2^{static}(t) = \frac{1}{35}[7 + 13\cos(6\omega_Q t) + 10\cos(12\omega_Q t) + 5\cos(18\omega_Q t)], \qquad (2.5)$$

in which $\omega_Q$ is the *quadrupole interaction frequency*. For half odd integer spin $\omega_Q$ is defined by[5]

$$\omega_Q = 6eQV_{zz} / 4I(2I-1)\hbar$$

The $G_2(t)$ function here is labeled "static" so as to be distinguished from the dynamic perturbation function to be introduced in the next section. $G_2(t=0)$ is always equal to 1. And for lattice sites with cubic symmetry the perturbation function is time independent: $G_2(t) = 1$, since no torque is exerted on the quadrupole moment. Finally if $^{111}$In/Cd probes occupy more than one sublattice, the resultant $G_2(t)$ function will be a superposition of the $G_2(t)$ functions for the individual sublattices, weighed by the fractions of probes staying on each sublattice.

### 2.1.4 Dynamic perturbation function and the XYZ model

The rare earth indides, gallides and aluminides studied in this work have the $L1_2$ structure, shown in Fig. 1. $^{111}$In/$^{111}$Cd probes naturally occupy the A-sublattice in the indides. In the gallides and aluminides the probe atoms were made to mostly occupy also the A-sublattice by making the sample deficient in A elements (see section 3.3). At A-sites the EFG is axially symmetric and perpendicular to the faces of the unit cell. Thus there are three orthogonal EFG directions, labeled as X, Y and Z in Fig. 1. The jump of a probe atom to a nearest neighbor site always results in reorientation of the EFG by 90º. Thus the probe experiences a fluctuating EFG instead of a steady one as it jumps. This leads to damping of the PAC spectrum and can be described by introducing a parameter $\lambda$ into the $G_2(t)$ function:

$$G_2(t) = e^{-\lambda t} G_2^{static}(t) \tag{2.6}$$

Winkler and Gerdau[7] first studied such a situation and developed a model later called the XYZ model[8]. Baudry and Boyer[9] obtained an empirical relation between $\lambda$ and the mean frequency at which the EFG changes to a single other orientation for a given probe ($w_{EFG}$). Approximate expressions of $\lambda$ were found for the *slow fluctuation regime* ($w_{EFG} \ll \omega_Q$) and the *fast fluctuation regime* ($w_{EFG} \gg 20\omega_Q$) respectively:

$$\lambda \simeq (N-1) w_{EFG} \quad \text{in slow fluctuation regime} \tag{2.7}$$

and

$$\lambda \simeq 100(\omega_Q / 6)^2 (1 / N w_{EFG}) \quad \text{in fast fluctuation regime,} \tag{2.8}$$

where N is the number of different orientations of the EFG. No analytic expression can be

given for the intermediate regime ( $\omega_Q < w_{EFG} < 20\omega_Q$ ), where maximum damping occurs. The jump frequency of a probe atom $w$ is equal to the product of the frequency at which the EFG changes to a specific orientation and number of different EFG orientations that a probe can jump to, other than its original one. Therefore $w = (N-1)w_{EFG}$, so that for the slow fluctuation regime we have the simple relation $w = \lambda$.

### 2.1.5 Inhomogeneous broadening

Defects in samples cause distortion to the EFG, the degree of which differs for different probe atoms depending on their distance to the defect. This causes *inhomogeneous broadening* of the PAC spectrum, which can be described by

$$G_2^{static}(t) = \frac{1}{35}[7 + 13\cos(6\omega_Q t)\,\mathrm{e}^{-\frac{1}{2}\sigma t} + 10\cos(12\omega_Q t)\,\mathrm{e}^{-\sigma t} + 5\cos(18\omega_Q t)\,\mathrm{e}^{-\frac{3}{2}\sigma t}], \qquad (2.9)$$

where $\sigma$ is a parameter that describes the degree of inhomogeneous broadening. $\sigma$ was found to be less than ~ 1 Mrad/s in all the samples studied in the present work. When fitting the spectrum, it is difficult to separate the damping caused by inhomogeneous broadening from that caused by dynamic broadening, and thus only one parameter, namely $\lambda$, was used in the fitting to describe the damping. Therefore the fitted value of $\lambda$ may be slightly higher than its true value. This effect can be ignored when $\lambda$ is large, but may be important at low temperature.

## 2.2 Diffusion mechanisms and point defects in $L1_2$ phases

This section will briefly discuss possible diffusion mechanisms feasible in $A_3B$ compounds of $L1_2$ type. We are mainly concerned with the majority constituent diffusion, since probe atoms mostly occupy the A-sublattice.

(1) The most elementary diffusion mechanism is an *A-monovacancy mechanism*. Probe atoms can diffuse as a consequence of random walks of A-vacancies ($V_A$) on their own sublattice. The jump frequency of probe atoms is proportional to the concentration of A-vacancies [$V_A$], the number of near neighbor A sites $z$ and the rate of exchange between an A-vacancy and a neighboring probe atom $w_2$:

$$w = z[V_A]w_2 \tag{2.10}$$

For this mechanism, the probe jump frequency can be related to the macroscopic quantity diffusivity $D$ by[10]

$$D = \frac{1}{6} f d^2 w \tag{2.11}$$

where $d$ is the jump length ($1/\sqrt{2}$ of lattice parameter) and $f$ is the *correlation factor*, which is between 1 and 0 and accounts for the nonrandomness of direction selection when a probe atom jumps. For vacancy self-diffusion on the A-sublattice $f$ is equal to 0.689[11], and for impurity diffusion it is a function of temperature and can be calculated using the *five frequency model*[12].

(2) A similar mechanism is the *divacancy mechanism*. Two monovacancies $V_A$ and $V_B$ can combine to form a divacancy due to energy advantage. The two members of the vacancy pair then move together but always on their own sublattice, leading to probe migration. Generally the concentration of divacancy rises faster than that of monovacancy[10] and is thus more important at high temperature. However the long

distance jump required of $V_B$ in the $L1_2$ structure makes the migration of divacancies difficult to happen.

(3) A *six jump cycle mechanism*[12] could also lead to $^{111}$Cd probe migration. Fig. 5 shows an example of a B-vacancy six jump circle. Here a B-vacancy makes six consecutive jumps to near neighbor sites, resulting in the exchange of two B atoms and the exchange of the vacancy and an A atom. Similarly an A-vacancy six jump circle leads to exchange of two B atoms and migration of the A-vacancy.

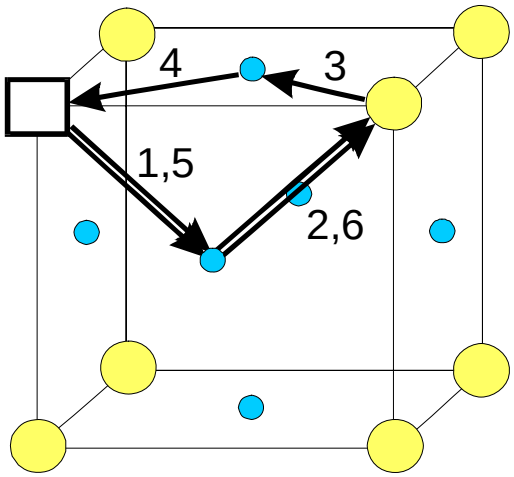


Fig. 5. Scheme of B-vacancy six jump cycle mechanism

(4) In a vacancy conversion mechanism, point defects may react with each other to form new types of point defects, if such a reaction can lead to lower total free energy. The reaction that concerns us here is $V_B + In_A \rightarrow A_B + V_A$, in which B-vacancies are converted into A-vacancies and thus contribute to the diffusion on the A-sublattice through the A-monovacancy mechanism.

(5) Zener[13] proposed the *ring exchange mechanism* for bcc and fcc metals, in which two or more atoms jump simultaneously on a ring to their near neighbor sites. It is

possible to think of 2-ring, 3-ring or 4-ring diffusion (Fig. 6) in fcc metals. The exchange mechanism is usually dismissed as an unrealistic picture since direct exchange of neighboring atoms in a close-packed crystal would cause great distortion of the lattice and require considerable amount of energy.[10] Zener showed in his early calculation for Cu metal that 3-ring and 4-ring diffusion are much less energetically costly per atom than 2-ring diffusion (the direct exchange of two atoms) and thus might be a feasible mechanism in the fcc structure, with the 4-ring mechanism requiring the lowest energy of all. [13]

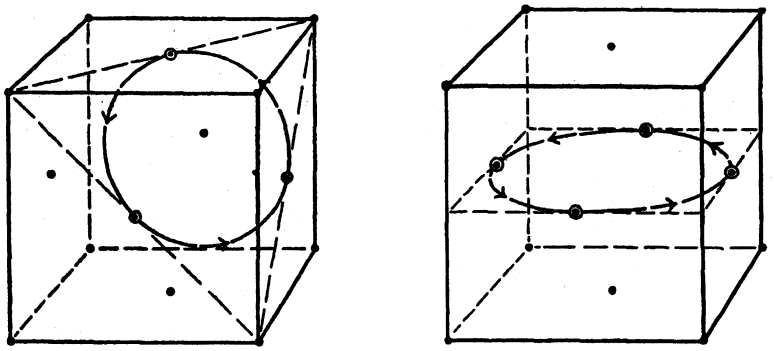

Fig. 6. Scheme of 3-ring and 4-ring diffusion in fcc metals (taken from Ref.13)

Except for the ring exchange mechanism, all the other mechanisms mentioned above are vacancy-mediated, which justifies a short discussion of point defects in solids. At least four types of point defects can form in ordered binary intermetallics, namely vacancies defects $V_A$ and $V_B$, and anti-site defects $B_A$ and $A_B$. The most likely defect to form in $L1_2$ crystals is probably a five-defect:

$$0 \rightarrow 4V_A + B_A, \tag{2.12}$$

with equilibrium constant

$$K_5 = [V_A]^4[A_B] = \exp(-G_5 / k_B T), \tag{2.13}$$

in which $[V_A]$ is the mole fraction of vacancies on the A-sublattice, etc. At stoichiometry, $[A_B] = \frac{3}{4}[V_A]$, so that one has

$$[V_A] \equiv C_0 \exp(-G_F^{eff} / k_B T) = (3/4)^{1/5} \exp(-G_5 / 5k_B T), \tag{2.14}$$

where $C_0$ is a constant and $G_F^{eff}$ is the effective free energy of formation of an A-vacancy.

At nonstoichiometry, structural defects arise to compensate for the deviation form stoichiometry. These defects could be the dominant type of defects when the compound is sufficiently off-stoichiometry and when temperature is not too high. It can be shown by thermodynamic consideration that $[V_B]$ and $[A_B]$ increase monotonically, and $[V_A]$ and $[B_A]$ decrease monotonically as the compound becomes more A-rich.[14]

# 3. Experimental methods

## 3.1 PAC instrumentation[15]

A typical planar 4-detector configuration is used to collect coincidence spectra. The arrangement of detectors and electronics is shown in Fig. 7. Four $BaF_2$ detectors are set around a sample at 90º intervals, each generating a fast signal and a slow signal when a gamma ray is detected. The fast signals are sent to a time-to-amplitude converter (TAC) so that the time interval between the detection of gamma rays can be recorded. Detectors 1 and 2 are used to start the TAC and detectors 3 and 4 to stop it. In the cases where one of the "start detectors" receives the first gamma ray and one of the "stop detectors" receives the second gamma ray, a "negative time" is recorded, giving rise to a negative side of the coincidence rate curve (Fig. 8). This helps to maximize the use of radiations, and is made possible by delaying the signal from the "stop detectors" by ~1μs. The negative-time data is completely analogous to positive-time data.

The slow signals from each of the four detectors are sent to an amplifier (AMP) and then to two single-channel analyzers (SCA). The SCAs determine whether the gamma ray is the 171eV one or the 245eV one and send this information to a routing logic unit. If a correct coincidence is confirmed by the logic unit, the signal in TAC is sent to an analog to digital converter (ADC) and then to a multichannel analyzer (MCA), where the time differences are histogrammed and from where the data can be accessed by a computer.

Four coincidence spectra are obtained, namely $C_{13}$, $C_{14}$, $C_{23}$, $C_{24}$, the subscript

corresponding to the detector pairs. They are stored in different portions of the MCA memory and the routing logic unit decides which portion to add new data to. An example of such coincidence spectrum is given in Fig. 8.

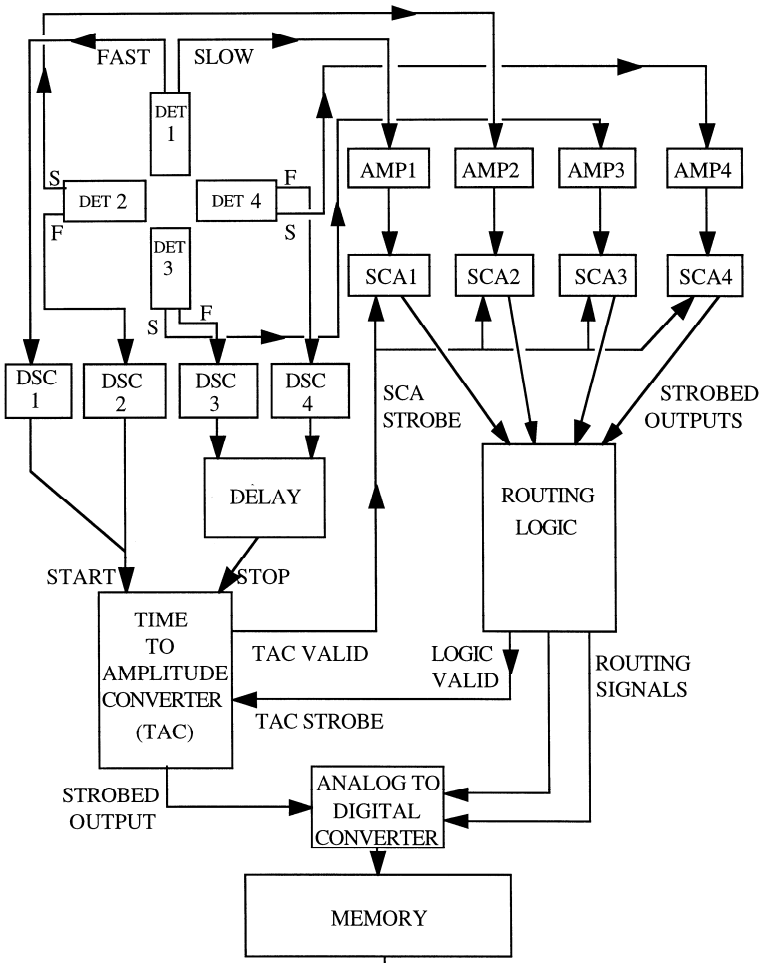


Fig. 7. Diagram of PAC electronics (taken from Ref.16)

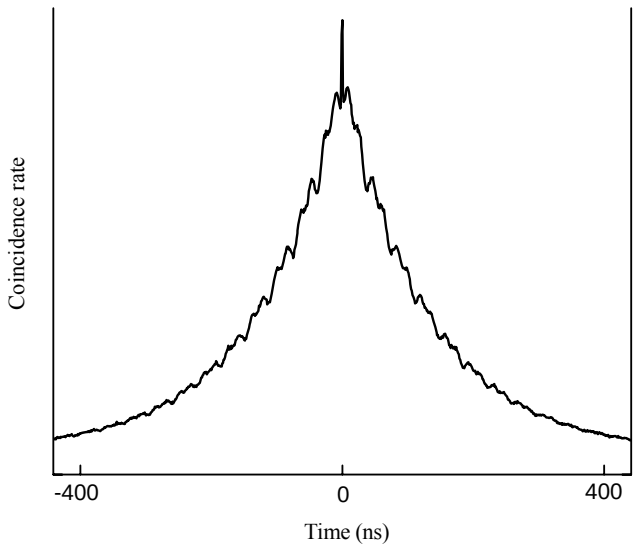


Fig. 8. Coincidence rate curve of $^{111}$In/Cd in ferromagnetic iron for two detectors at 180°

### 3.2 Data reduction[17]

For actual experiments, Eq.(2.2) is modified by an angular attenuation factor $\gamma_a$ which accounts for the solid angles that the detectors subtend to the sample:

$$W(\theta,t) = 1 + A_2\gamma_a G_2(t) P_2(\cos\theta). \tag{3.1}$$

$\gamma_a$ was about 0.7 in our experiments. (The $A_4G_4(t)$ term is omitted as it is not detected for the 4-detector configuration mentioned above.) The coincidence rate curve shown in Fig. 8 can be described by

$$C_{ij}(\theta,t) = \overline{C}_{ij}(\theta,t) + B_{ij} = N_{ij}e^{-t/\tau}W(\theta,t) + B_{ij}, \tag{3.2}$$

in which the first term is the true coincidence rate and $B_{ij}$ is a background caused by accidental (false) coincidences, $e^{-t/\tau}$ describes the lifetime decay of the intermediate state and $N_{ij}$ is the product of the activity $A$, accumulation time $T$, detector efficiencies $e_i$ and $e_j$, and solid angles $\Omega_i$ and $\Omega_j$ for detector pair (i, j):

$$N_{ij} = e_i e_j \Omega_i \Omega_j A T \tag{3.3}$$

During data reduction, $C_{ij}(\theta,t)$ is first fitted with an exponential decay plus a constant so that $\overline{C}_{ij}(\theta,t)$ is obtained. $G_2(t)$ can then be calculated from $\overline{C}_{ij}(\theta,t)$ by

$$G_2(t) = \frac{2}{\gamma_2 A_2} \cdot \frac{\sqrt{\overline{C}_{13}(180^\circ,t)\overline{C}_{24}(180^\circ,t)} - \sqrt{\overline{C}_{14}(90^\circ,t)\overline{C}_{23}(90^\circ,t)}}{\sqrt{\overline{C}_{13}(180^\circ,t)\overline{C}_{24}(180^\circ,t)} + 2\sqrt{\overline{C}_{14}(90^\circ,t)\overline{C}_{23}(90^\circ,t)}}. \tag{3.4}$$

It can be seen from Eq.s (3.2) and (3.3) that detector efficiencies and solid angles cancel out in Eq.(3.4).

### 3.3 Sample preparation

Samples were made of $PrIn_3$, $NdIn_3$, $GdIn_3$, $TmIn_3$, $DyGa_3$, $ErGa_3$, $LuGa_3$ and $ErAl_3$ by arc melting the two constituent metals. High purity metal foils were carefully cleaned to remove dirt and oxide on the surface. They were then cut and weighed out to achieve the desired composition. A few microliters of radioactivity in the form of $^{111}InCl_3$ dissolved in 0.05M HCl solution were dried on one of the metal foils. The two foils were then folded and compressed into one piece. Melting was conducted in a sealed arc furnace. Before melting, gases in the furnace interior were purged with research grade argon gas for at least 10 minutes to create a non-oxidizing atmosphere. Sample was then

melted by passing through it a DC current of 45A or 55A for ~1sec, depending on the melting point of the metals involved. Sample was then turned over and melted once more for ~1sec. The thus obtained sample was usually in a spherical shape, indicating that the two constituent metals had fully mixed.

Each sample was weighed again after the melting and the mass loss was calculated. The composition range of the sample was then calculated by assuming the mass loss was entirely due to loss of one constituent or the other. The masses of the samples were between 40 mg to 80 mg and mass losses were between 1mg to 4 mg. Compared with arc melting of many rare earth-aluminum alloys, in which mass losses were usually less than 1 mg, the relatively large mass losses in gallide and indide samples were most likely caused by evaporation of gallium and indium during melt, as these two elements have high vapor pressures.

$A_3B$ samples were prepared to have either A-rich or A-poor mean compositions, usually a few percent away from the stoichiometry. So the actual samples were a mixture of the desired $A_3B$ phase and a small amount of its adjacent phases.

### 3.4 Measurement at high temperature

Spectra were collected from RT to 1200 K. High temperature measurement was carried out in a high vacuum (~$10^{-8}$ mBar) chamber. The sample was heated by three tungsten filaments about 1 cm away from it and was in touch with a K-type or R-type thermocouple which was used to measure and control the temperature. The high temperature and high vacuum environment could lead to significant In or Ga evaporation for some samples and could give rise to two problems: 1, The sample tends to lose In or Ga over time and its composition changes. 2, $^{111}$In/Cd probes that diffuse into the wall of the vacuum chamber can produce an artificial cubic signal. In order to reduce evaporation, samples were wrapped in 0.001 inch thick iron foil. Iron was chosen because indium is insoluble in it and indium and iron liquids are immiscible. Coincidence spectra were collected for ~24 hours per measurement for most samples, and for ~ 8 hours per measurement for samples which tend to have significant In outdiffusion.

# 4. Results

## 4.1 $PrIn_3$

$PrIn_3$ samples were prepared at both phase boundaries A and B. The adjacent phases of $PrIn_3$ are pure In and $Pr_3In_5$ (Fig. 9). Sample A had nominal composition range of 24.2 at.% to 27.1 at.% Pr. Although this range encompassed 25.0 at.% Pr, the sample was determined to have an In-rich mean composition because a signal from In metal phase was identified in the first measurement at room temperature (RT). The less In-rich sample had nominal composition range of 26.2 at.%-27.9 at.% Pr.

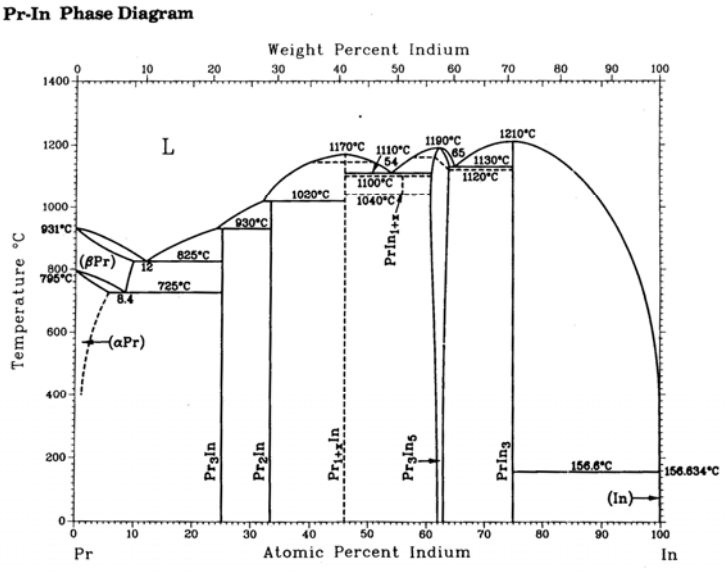


Fig. 9. Phase diagram of Pr-In system (taken from Ref. 18)

The left portion of Fig. 10 shows representative PAC spectra of the $PrIn_3$ (A)

sample in the slow fluctuation regime. The solid lines were perturbation functions fitted with (a superposition of) Eq.(2.6). The spectrum at RT fits with a signal of 58(2)% fraction with the *fundamental frequency* $\omega_0 \equiv 6\omega_Q = 74.0(1)$ Mrad/s, and a signal of 14(1)% fraction with $\omega_0 = 16.3(5)$ Mrad/s, both of which are axially symmetric. The majority signal is attributed to $^{111}$In/Cd probes on the In-sublattice of $PrIn_3$. The minority signal agrees very well with the hyperfine interaction frequency of Cd in pure In metal at RT: $\omega_0 = 16.80(1)$ Mrad/s [19], proving the sample to be indeed at the more In-rich phase boundary. The spectrum at 805 K shows a typical static perturbation function, described by Eq.(2.5), with very little inhomogeneous broadening. The 34.1(1)% offset in this spectrum could be attributed to probes in liquid In and in the oven's inner wall. As temperature increases, motion of Cd probes leads to more and more damped spectra, as observed in the measurements at 975 K and 1018 K. The spectrum at 1125 K approaches the intermediate regime where the maximum damping occurs. Evaporation of In renders measurement in the fast fluctuation regime impossible.

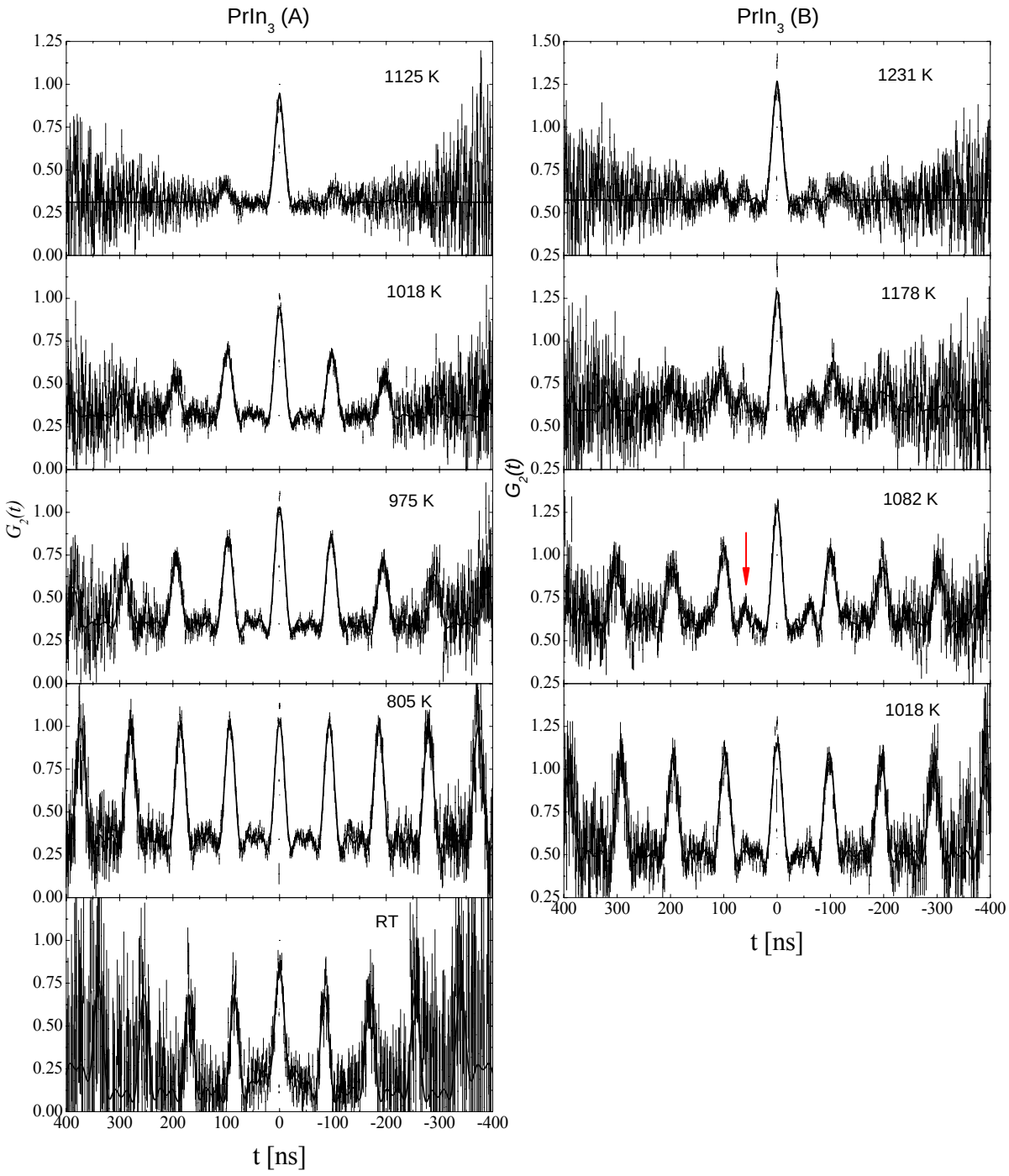


Fig. 10. PAC spectra of $PrIn_3$ at phase boundary compositions A and B. Solid lines are best fits of perturbation functions. The arrow indicates a signal from the adjacent $Pr_3In_5$ phase.

The spectra of $PrIn_3$ (B) sample (Fig. 10 right) fit with two signals. The dominant signal is identical to the high frequency signal in the sample A and is naturally attributed to probes on the In-sublattice of $PrIn_3$. The other signal (indicated by arrow in Fig. 10) has a fundamental frequency $\omega_0 = 100.0(5)$ Mrad/s and $\eta = 0.929(7)$ at 1082 K, and is attributed to probes in the neighboring phase $Pr_3In_5$. It takes about 100 K increase in temperature for sample B to show the same amount of damping as sample A does.

The fitted values of $\lambda$ (equal to jump frequency $w$) are shown in Fig. 11. The three measurements at high temperature of the B sample fall on a straight trend line. The deviation of the two measurements at lower temperature could be explained by misfit due to inhomogeneous broadening.

The sequence of measurement on the A sample is numbered in Fig. 11 (The first measurement at RT is not included). The first four measurements fall on a straight trend line. The 5$^{th}$ and 6$^{th}$ measurements fall below this trend line, opposite to what one would expect if there was inhomogeneous broadening. The 7$^{th}$ approached the trend line of the B sample, and the last three measurements fall very well on it. This could be understood by taking into consideration the volatility of Indium. High temperature and high vacuum condition caused In to evaporate out of the In-rich sample, turning it from the A phase boundary to the B phase boundary, and thus moved $w$ from one trend line toward the other. This change of behavior and the consistency of the last three measurements of the B sample with those of the A sample is further proof that the two samples were indeed at the less In-rich and more In-rich phase boundaries respectively. The straight lines in Fig. 11 are jump frequencies fitted with an Arrhenius temperature dependence

$$w = w_0 \exp(-Q / kT), \tag{4.1}$$

in which $w_0$ is a prefactor and $Q$ is the activation enthalpy for Cd probes to jump. Points 1-4 were used in the fitting for the A boundary. Points 8-10 together with the three triangle points at high temperature were used in the fitting for the B phase boundary. The best fit values of $w_0$ and $Q$ are listed in Table 1.

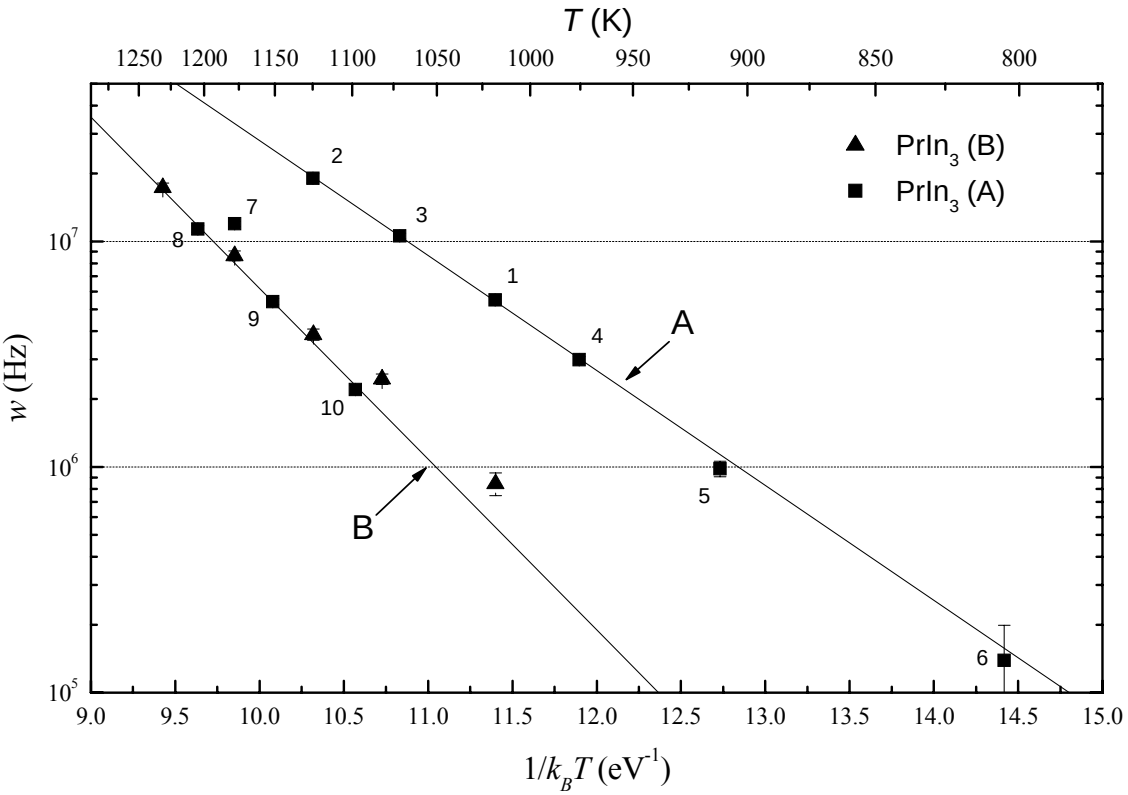


Fig. 11. Arrhenius plot of Cd jump frequencies in $PrIn_3$ at two phase boundaries and their best fits. The numbers designate the order of measurement on the B sample.

## 4.2 $NdIn_3$

Jump frequencies were measured in $NdIn_3$ for both phase boundaries A and B. The sample A had nominal composition range 15.8-19.9 at.% Nd. And like in $PrIn_3$ (A), a signal corresponding to In metal was observed at RT ($\omega_0 = 17.0(3)$ Mrad/s), proving its mean composition to be In-rich. The sample B (composition range 22.0-30.8 at.%.) showed a majority signal of $\omega_0 = 62.95(9)$ Mrad/s and a minority signal (pointed by arrow in Fig. 13) of $\omega_0 = 98.8(4)$ Mrad/s, $\eta = 0.94(1)$ at 1064 K, which is attributed to the neighboring phase $Nd_3In_5$ for two reasons: (1) It is very similar to the minority signal seen in $PrIn_3$ (B). (2) The percentage of this signal increased gradually during high temperature measurements, which could be explained by the increase of $Nd_3In_5$ fraction

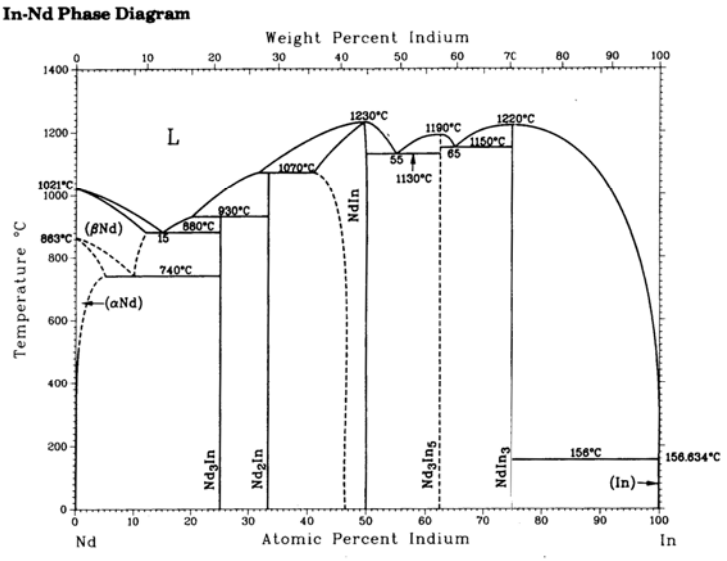


Fig. 12. Phase diagram of Nd-In system (taken from Ref. 18)

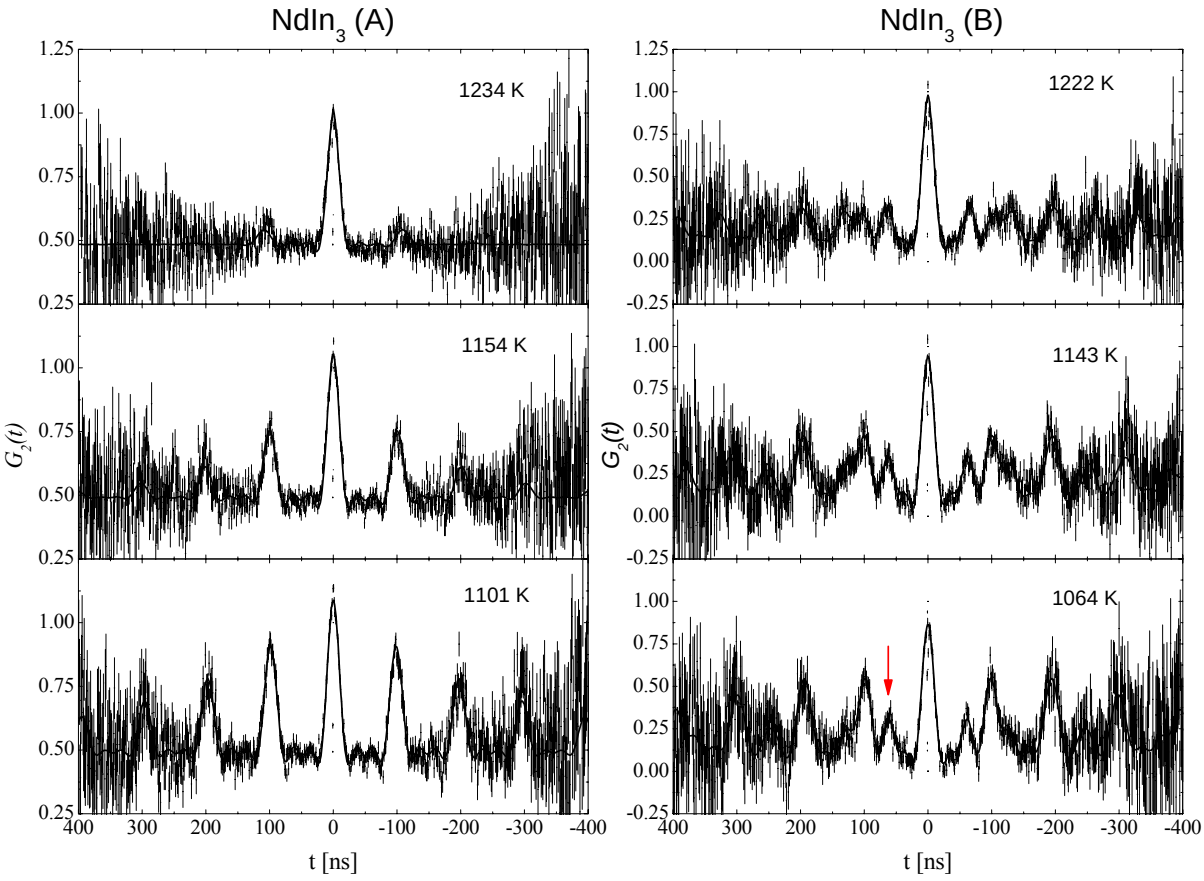


Fig. 13. PAC spectra of $NdIn_3$ at opposing phase boundaries A and B, and the best fits of perturbation functions. The arrow indicates a signal from the adjacent $Nd_3In_5$ phase.

due to In evaporation. Thus one can conclude that the sample B indeed had an In-poor mean composition.

PAC spectra of both $NdIn_3$ (A) and $NdIn_3$ (B) samples are shown in Fig. 13. Damping is seen above about 1000 K and reaches the intermediate regime at about 1250 K. Jump frequencies are very close in the two samples (see Fig. 14). The solid lines in Fig. 14 are Arrhenius fits of the jump

frequencies, each fitted to 5 points. The lowest triangular point deviates from the fit for the composition boundary B due to inhomogeneous broadening, and was thus not included in the fitting.

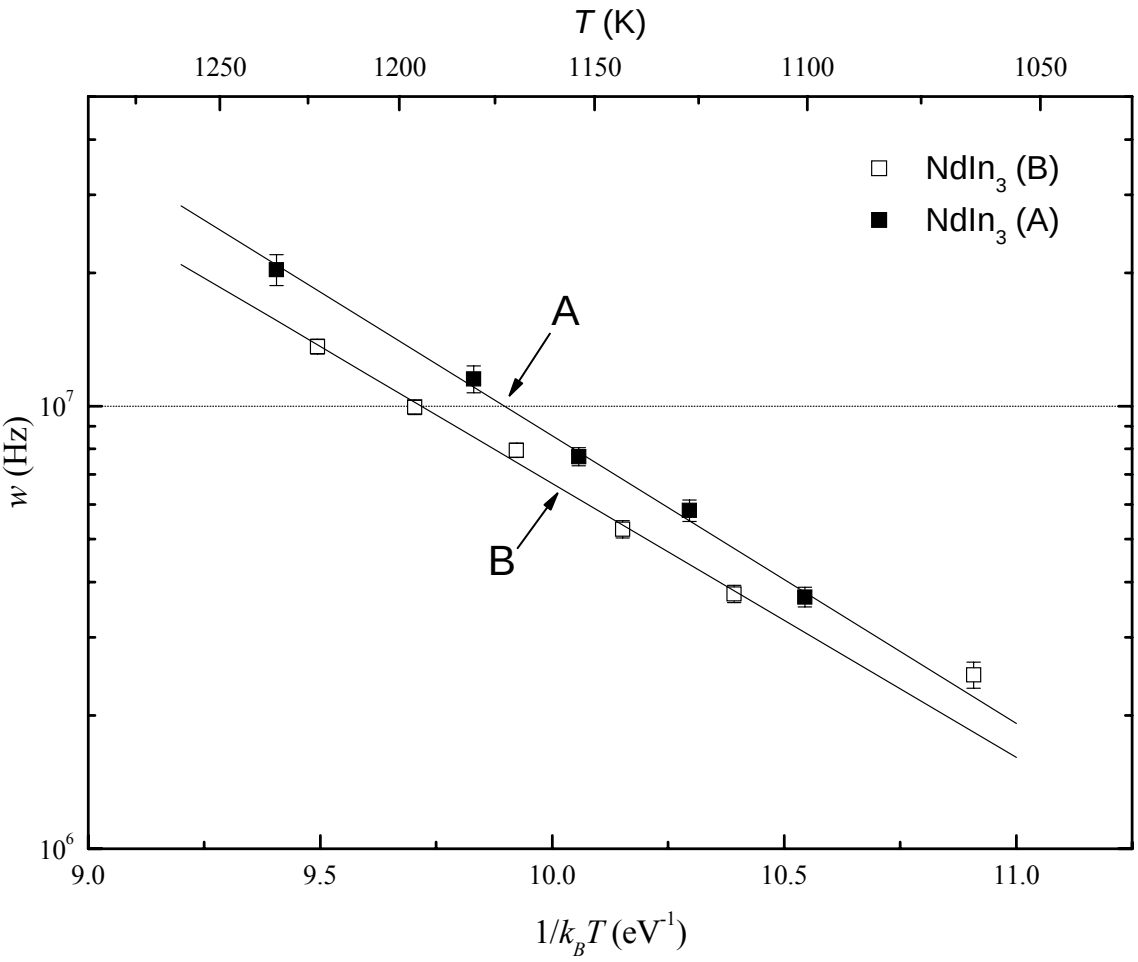


Fig. 14. Arrhenius plot and of Cd jump frequencies in $NdIn_3$ at two phase boundaries and their best fits.

### 4.3 $TmIn_3$

The adjacent phases of TmIn3 are Tm3In5 and In (Fig. 15). Like in PrIn3 and NdIn3, jump frequency was measured on the two opposing phase boundaries for TmIn3, and minority signals from adjacent phases were used to verify the mean compositions of the samples. The results are summarized in Fig. 16.

The jump frequencies in the In-poor sample fall very well on a straight trend line. The temperature dependence of jump frequency was fitted using the 5 unfilled points at higher temperatures. The lowest unfilled point deviates from the fit slightly, which is most likely due to inhomogeneous broadening.

Jump frequencies were measured in three In-rich samples. Significant In outdiffusion was seen in the first two samples (not shown), which interfered with jump frequency measurements. To reduce In loss, the third sample (shown in Fig. 16) was run for shorter period (~8 hours) per measurement, and thus has relatively large error bars. The 6 filled points at lower temperatures fall on a trend line and were used in the fitting for the temperature dependence. The filled point at the highest temperature (the last run) agrees very well with the fit for the In-poor sample, which suggests that the composition of the sample had changed into In-poor by the time of this measurement.

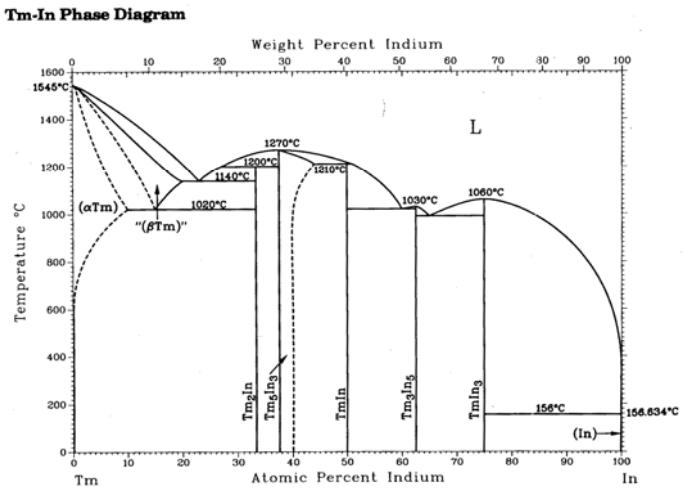


Fig. 15. Phase diagram of Tm-In system (taken from Ref. 18)

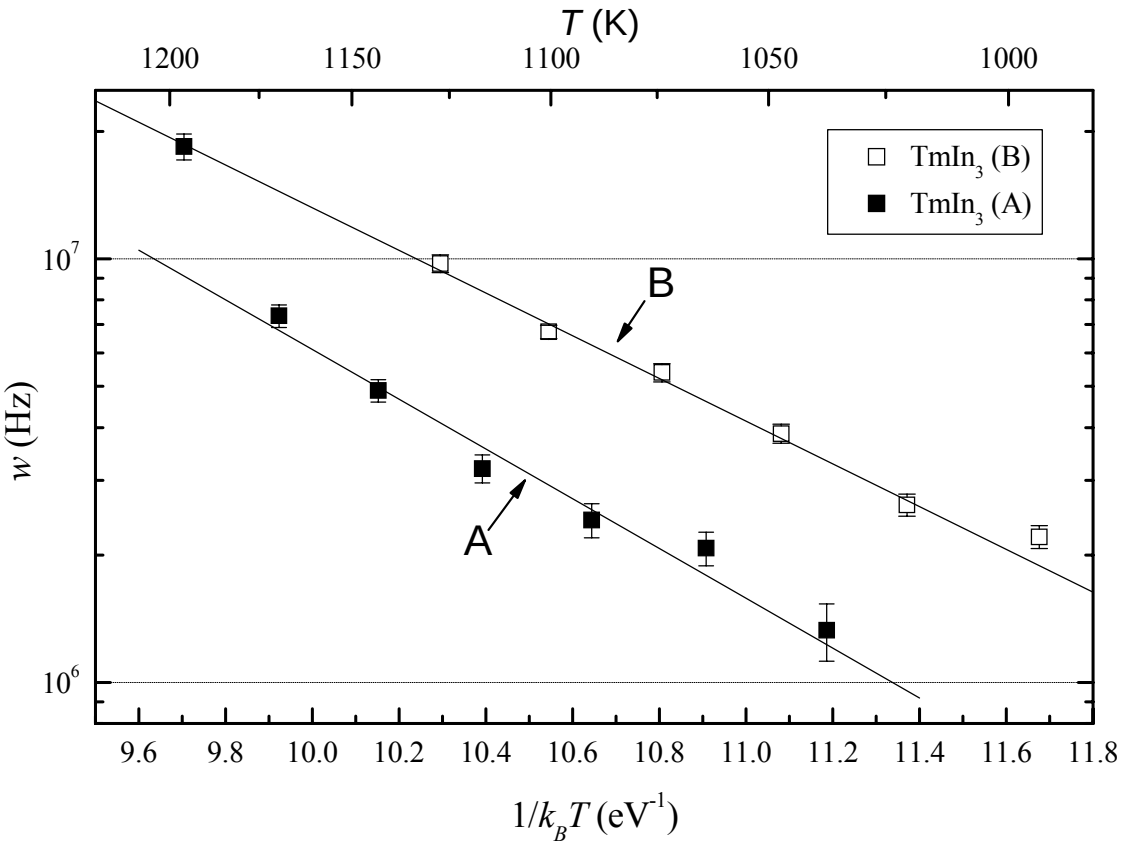


Fig. 16. Arrhenius plot of Cd jump frequencies in $TmIn_3$ at opposing phase boundaries and their best fits.

### 4.4 $GdIn_3$

The results of jump frequency measurements in $GdIn_3$ at both boundary compositions are shown in Fig. 17. Like in $TmIn_3$, measurements in the In-rich sample were made for 8-hour periods to reduce In evaporation. All the 7 square points fall very well on a straight line and were used in the fitting for the boundary B. With only 4 triangular points sitting close to a trend line, it is difficult to tell if the composition of the sample A had changed during measurement, and thus the fitting is less reliable for the boundary A. Nevertheless it is clear that the jump frequency is much lower at phase boundary A than at phase boundary B.

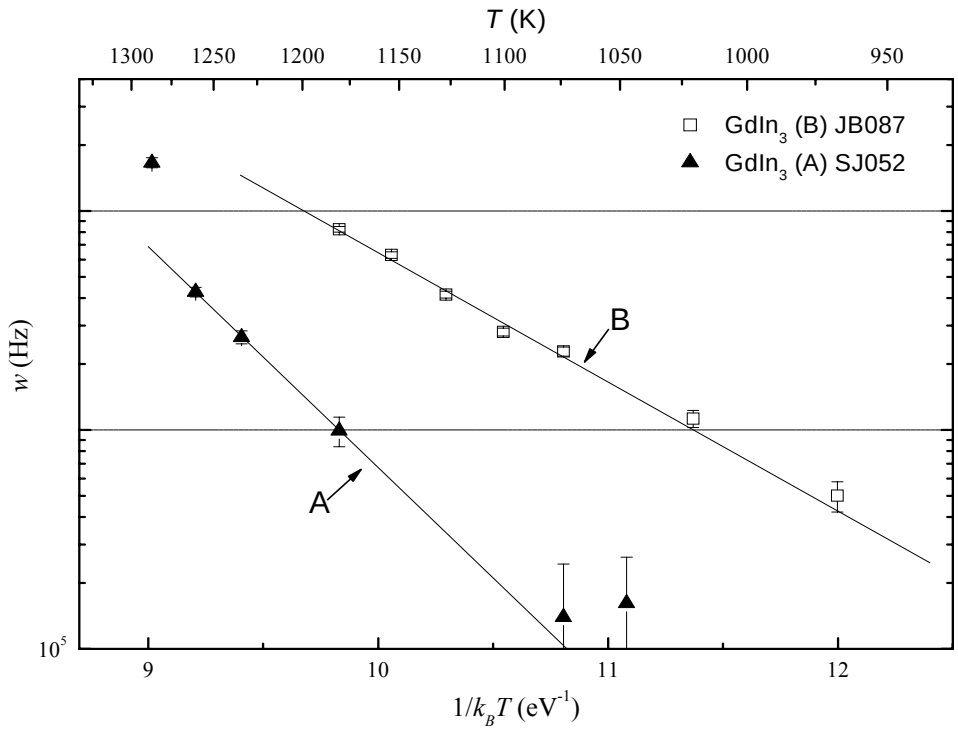


Fig. 17. Arrhenius plot of Cd jump frequencies in GdIn3 at opposing phase boundaries and their best fits.

### 4.5 $DyGa_3$, $ErGa_3$, $LuGa_3$ and $ErAl_3$

Cd jump frequencies were also measured in $DyGa_3$, $ErGa_3$, $LuGa_3$ and $ErAl_3$ at the B phase boundaries. In these compounds, In is no longer a host element and nonstoichiometry of the sample would drive $^{111}$In/Cd probes to occupy the sublattice of which the host element is deficient.[20] Therefore at the B phase boundaries, $^{111}$In/Cd probes tend to occupy the desired non-cubic sites, as demonstrated in Fig. 18. While at the A phase boundaries $^{111}$In/Cd probes would be driven to the cubic rare earth sites, rendering jump frequency measurement difficult to impossible. This was confirmed by measurements on two $ErGa_3$ (A) samples, in which less than 10% of the probes showed periodic hyperfine interaction (not shown).

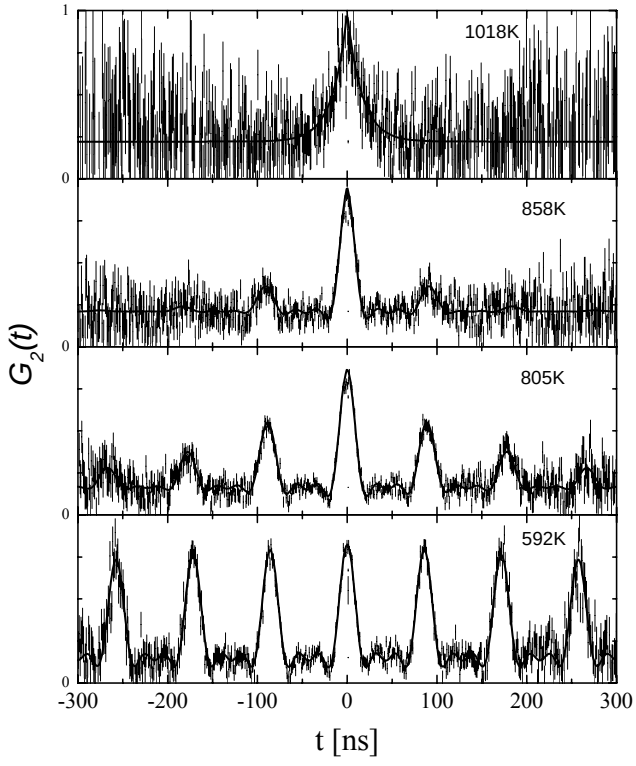


Fig. 18. PAC spectra of $ErGa_3$ (B).

Fig. 18 shows representative PAC spectra and fitted perturbation functions of $ErGa_3$ (B). The three spectra at the bottom exhibited typical behavior in the slow fluctuation regime, where damping increases with temperature. The spectrum on the top is an example of behavior in the fast fluctuation regime, where the periodic interaction is no longer visible and the damping decreases with temperature. Similar spectra were obtained for $DyGa_3$, $LuGa_3$ and $ErAl_3$ in the slow fluctuation regime, however damping in these phases was seen at much higher temperature. The jump frequencies in all the four phases and the fits to Arrhenius temperature dependence are shown in Fig. 19. Only points that fall close to the straight lines were used in the fitting. The fitted values of $Q$ and $w_0$ are listed in Table 1. Jump frequencies in all the four samples deviate from their trend lines at low temperatures. This could be caused by inhomogeneous broadening due to distant defects. It is also possible that there exists a second jump mechanism, which has much lower an activation enthalpy and thus is not visible at high temperature but becomes important at low temperature.

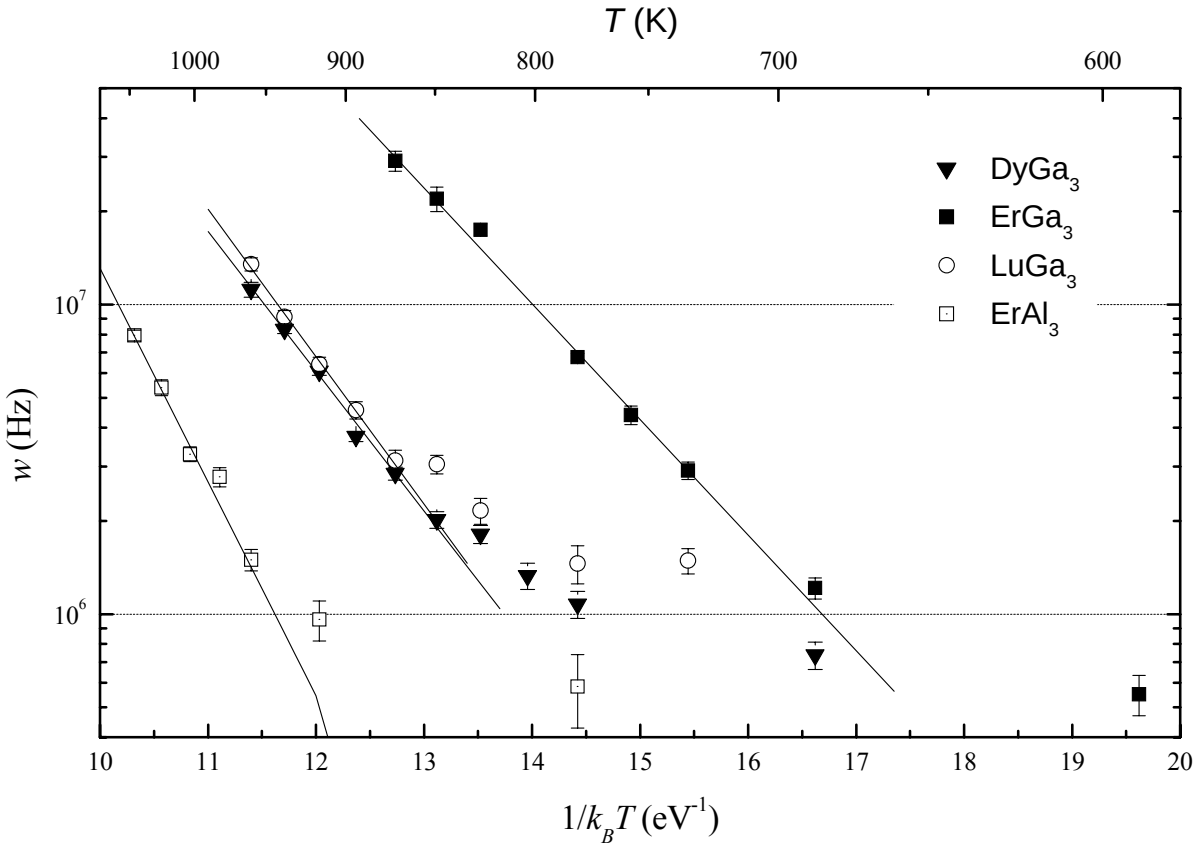


Fig. 19. Arrhenius plot of Cd jump frequencies in $DyGa_3$, $ErGa_3$, $LuGa_3$ and $ErAl_3$ at the B phase boundary and their best fits.

# 5. Discussion

## 5.1 Cd jump frequencies in various $L1_2$ intermetallics

Fig. 20. summarizes the jump frequencies of Cd in $L1_2$ type rare earth indides, gallides, stanides, and aluminides measured by PAC in this work and in previous works [4, 21]. Jump frequencies in all these phases exhibit the Arrhenius behavior and the fitted values of activation enthalpies and prefactors are listed in Table 1. Jump frequencies at 1200 K span a large range from ~6000 MHz in $LaIn_3$ (A) to less than 1 MHz in $ScAl_3$. Most phases show jump frequencies in the range of 1 – 10 MHz at 1000 K, which can be translated into diffusivities in the range of $10^{-14} - 10^{-13}\ m^2/s$ using Eq.(2.11). Most activation enthalpies are between 0.8 and 1.8 eV. The jump frequencies are high and activation enthalpies are low compared with diffusion in other metallic systems.[10, 12, 22] A few phases such as $LaIn_3$ and $ErGa_3$ have remarkably low activation enthalpies. Cd and In are very similar in their chemical properties and atomic radii, and thus one could expect the diffusion of Cd probes in indides not to be too much different from the self diffusion of In. Therefore the measurements suggest similar high self diffusion coefficients for In in rare earth indides.

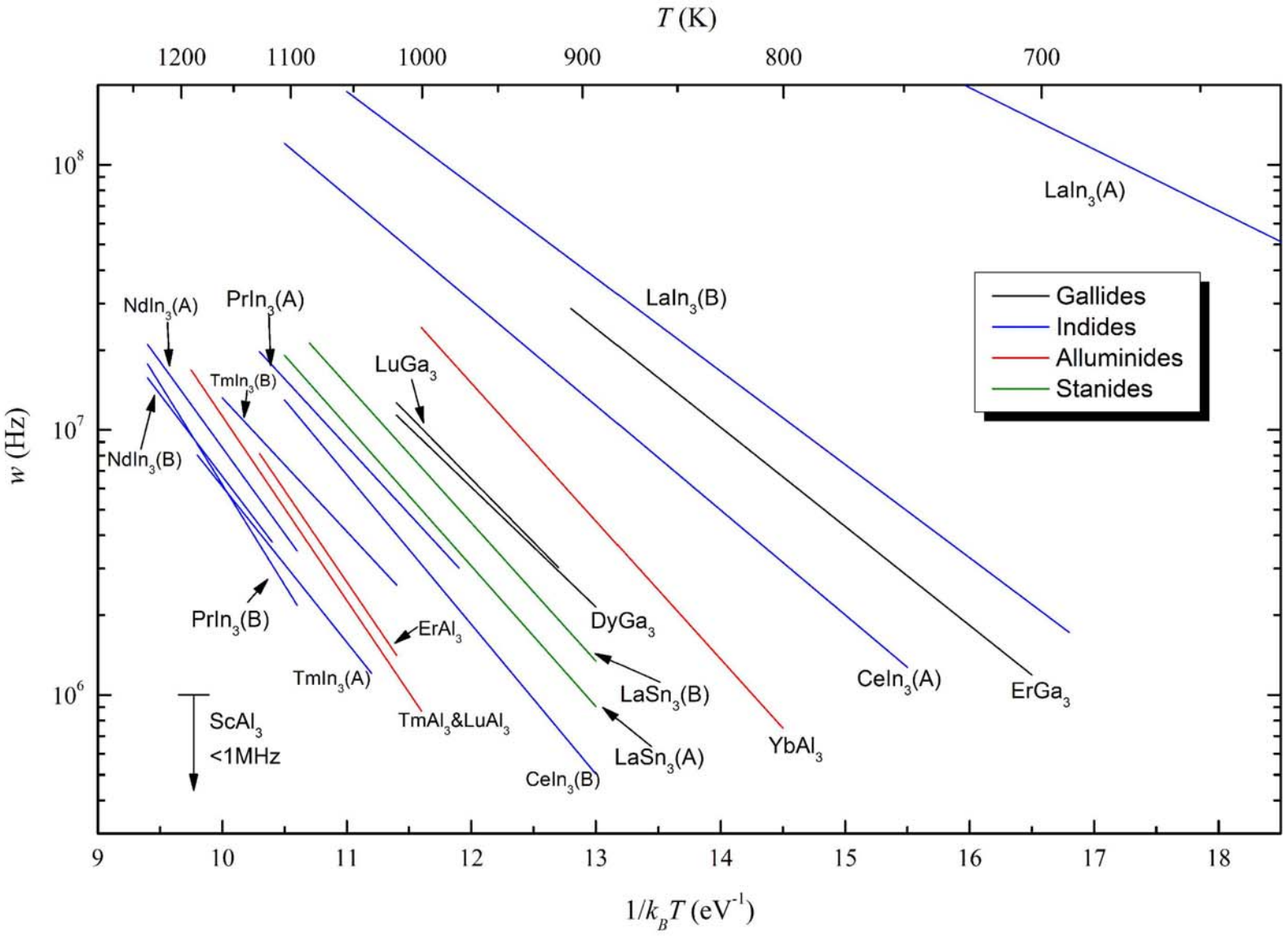


Fig. 20. Cd jump frequencies in various L12 intermetallics measured by PAC

Table 1. Prefactors and activation enthalpies for Cd jump in various $L1_2$ phases. Composition is unknown if not listed.

| Phases | $Q$ [eV] | $w0$ [THz] | Lattice Parameter[23] [Å] | Source of Data |
|---|---|---|---|---|
| $DyGa_3$ (B) | 1.04(9) | 1.6(1.7) | 4.271 | This work |
| $ErGa_3$ (B) | 0.86(5) | 1.7(1.3) | 4.206 | This work |
| $LuGa_3$ (B) | 1.10(6) | 3.5(2.5) | 4.180 | This work |
| $ErAl_3$ (B) | 1.6(2) | 106(208) | 4.215 | This work |
| $TmAl_3$ | 1.6(1) | 100(+100,-50) | 4.200 | [19] |
| $LuAl_3$ | 1.6(1) | 100(+100,-50) | 4.187 | [19] |
| $YbAl_3$ | 1.2(1) | 27(+17,-11) | 4.202 | [19] |
| $LaSn_3$ (A) | 1.22(5) | 7(+5,-3) | 4.769 | [4] |
| $LaSn_3$ (B) | 1.2(1) | 8(+21,-6) | | [4] |
| $LaIn_3$ (A) | 0.535(2) | 1.02(0.05) | 4.732 | [4] |
| $LaIn_3$ (B) | 0.81(1) | 1.4(0.2) | | [4] |
| $CeIn_3$ (A) | 0.91(4) | 1.7(+1.2,-0.7) | 4.691 | [4] |
| $CeIn_3$ (B) | 1.30(7) | 11(+13,-6) | | [4] |
| $PrIn_3$ (A) | 1.17(3) | 3.5(1.3) | 4.671 | This work |
| $PrIn_3$ (B) | 1.75(9) | 240(120) | | This work |
| $NdIn_3$ (A) | 1.50(9) | 27(25) | 4.653 | This work |
| $NdIn_3$ (B) | 1.4(1) | 10(10) | | This work |
| $GdIn_3$ (A) | ~2.3 | ~8000 | 4.607 | This work |
| $GdIn_3$ (B) | 1.36(1) | 5.2(4.5) | | This work |
| $ErIn_3$ (B) | 1.13(4) | 0.77(0.33) | 4.564 | This work |
| $TmIn_3$ (A) | 1.4(2) | 5(8) | 4.548 | This work |
| $TmIn_3$ (B) | 1.2(1) | 1.5(1.5) | | This work |
| $YIn_3$ | 1.43(5) | 34(+26,-15) | 4.592 | [4] |

The most striking observation is the great composition dependence of jump frequencies in some so called “line compounds”. For example, in $LaIn_3$, $CeIn_3$ and $PrIn_3$, jump frequencies differ by one to two orders of magnitude at the opposing phase boundaries. In addition, reversal of behavior is observed between the early and late rare earth indides: activation enthalpy is lower at the A phase boundary in $LaIn_3$, $CeIn_3$ and $PrIn_3$, about the same at both the boundaries in $NdIn_3$, and higher at the A boundary in $GdIn_3$ and $TmIn_3$ (see Fig. 21). The activation enthalpies in the three early rare earth indides appear to decrease smoothly with their lattice parameters, but the late rare earth indides do not continue this trend. These differences between the early and late rare earth indides strongly suggest that different diffusion mechanisms are operational in the two sets of phases.

Some late rare earth elements like Er, Tm, Lu and Yb are chemically alike and thus one would expect to see similar diffusional behavior in their compounds. The aluminides of the first three of these elements exhibit almost identical jump frequencies in the temperature range investigated, while $YbAl_3$ has jump frequencies larger by an order of magnitude. This may suggest that $YbAl_3$ has a much wider phase field than the other three phases, providing more structural defects to facilitate Cd migration.

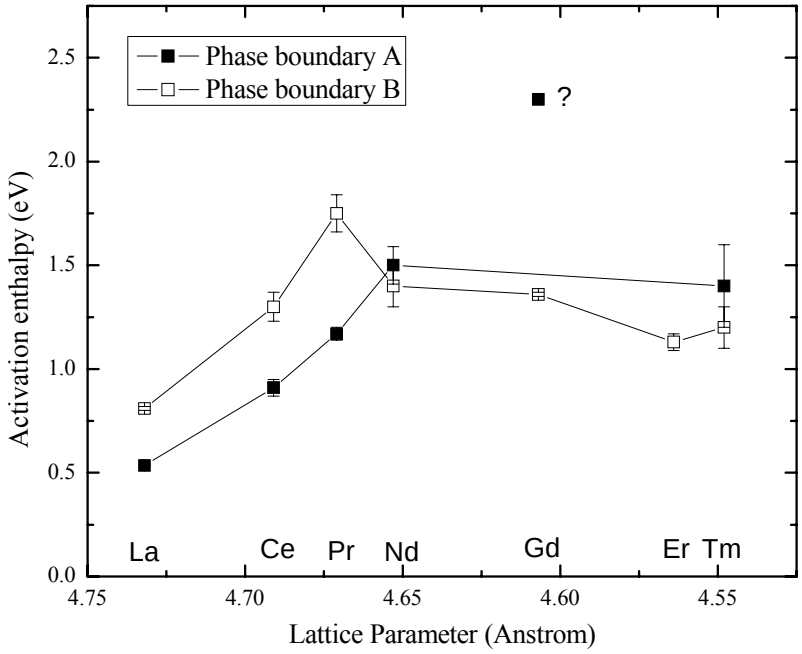


Fig. 21 Activation enthalpies of Cd jump in $RIn_3$ systems vs. lattice parameters. (The point with ? may be subject to systematic error.)

### 5.2 Actual compositions of the A and B phase boundaries

Although rare earth indide samples were made to have either In-rich (A) or In-poor (B) mean compositions, and were proven to be so by identifying signals from adjacent phases, the actual compositions of the $RIn_3$ phases do not necessarily have to be absolutely In-rich or In-poor accordingly, but depends on the shapes and relative positions of the free energy curves of the $RIn_3$ phase and its adjacent phases. Phase field boundaries are determined by the common tangents of the free energy curves of the phase in question and its neighboring phases (illustrated in Fig. 22). If the free energy curve of a

phase is sharp and has its minimum close to that of its next phase, then the phase boundary will be very close to stoichiometry; On the other hand if the free energy curve is less sharp and its minimum differs much from that of its next phase, then the phase boundary tends to be off stoichiometry. No ready information is available about the free energy curves of the rare earth - indium systems presently studied. However it is possible to make a rough estimation of the relative positions of the minima of these curves using the melting points of neighboring phases. The free energy of formation of a phase is $\Delta G_f = \Delta H_f - T\Delta S_f$, where $\Delta H_f$ and $\Delta S_f$ are the enthalpy and entropy of formation. If one ignores the difference in $\Delta S_f$, then $\Delta G_f$ could be roughly measured by the heat of formation (equal to $\Delta H_f$), which is decided largely by the melting point of the phase, if one further ignores the differences in the latent heat and the specific heat.

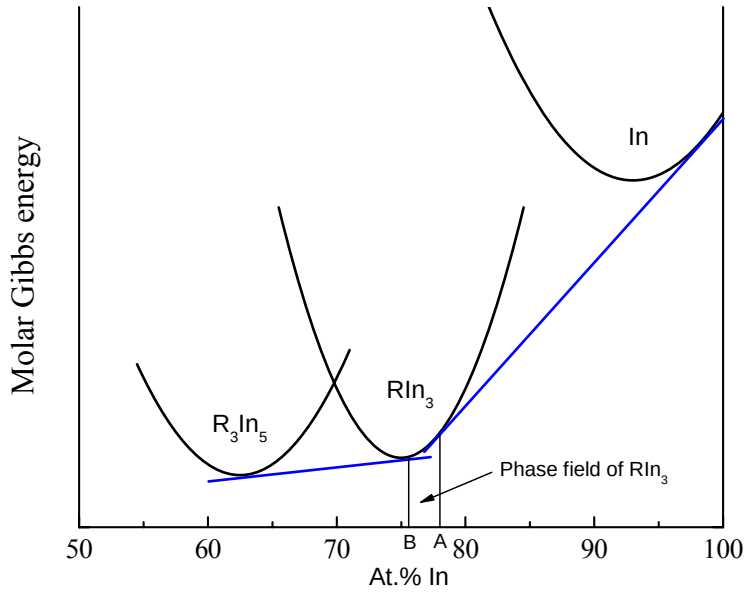


Fig. 22. Determination of phase boundaries of $RIn_3$ using free energy curves.

The phase diagrams of Pr-In, Nd-In and Tm-In are shown in Fig. 9, Fig. 12 and Fig. 15. The phase diagrams of La-In, Ce-In, Gd-In and La-Sn are not shown but are very similar to those shown in that all the $A_3B$ phases are adjacent to a high melting point phase $A_5B_3$ ($A_2B$ in the case of Ce-In) and a phase with very low melting point (In or Sn), with the melting point of $A_3B$ being very close to that of $A_5B_3$. Therefore, by the rough estimation developed above, we would expect the free energy curves of $A_3B$ and $A_5B_3$ to have close minima while the minimum of the pure B phase is well above the other two, as is depicted in Fig. 22. It then follows that the phase boundary B is very close to stoichiometry (may be slightly A-rich or A-poor) and the phase boundary A is indeed on the A-rich side and relatively far away from stoichiometry.

**5.3 Diffusion mechanisms**

As was suggested above, different diffusion mechanisms may prevail in the early and late rare earth indides. The most natural (and widely accepted) mechanism for the diffusion of the majority element would be the A-monovacancy mechanism, in which the $^{111}$In/Cd probe jumps on its own sublattice by fast passage of A-vacancies. In this mechanism, the jump frequency of Cd would be proportional to $[V_A]$, which itself increases monotonically as the composition of the sample moves from the phase boundary A to B. Therefore this mechanism is consistent with the observations in $GdIn_3$, $TmIn_3$ and $LaSn_3$, in which jump frequencies are higher at the B boundary. For this mechanism, one would expect the activation enthalpies at the A and B phase boundaries $Q_A$ and $Q_B$ to be approximately equal. Since $V_A$ is not a structural defect and has to be

thermally activated at both phase boundaries in the fashion of Eq.(2.14), one has

$$w \propto [V_A]\exp(-Q^m_{V_A} / k_B T) \propto \exp[-(Q^f_{V_A} + Q^m_{V_A}) / k_B T)],$$

in which $Q^f_{V_A}$ is the formation enthalpy of an A-vacancy and $Q^m_{V_A}$ is the enthalpy barrier that a probe atom has to overcome to migrate to an adjacent empty A-site. It follows that

$$Q_A = Q_B = Q^f_{V_A} + Q^m_{V_A}$$

This interpretation is supported by the fact that the measured activation enthalpies in $TmIn_3$ and $LaSn_3$ at the two phase boundaries are fairly close (see Table 2). $GdIn_3$ is not included in Table 2 because reliable *Q* value was obtained for only one phase boundary.

The early rare earth indides have higher jump frequencies and lower activation enthalpies at the more In-rich phase boundary, and consequently require more complicated jump mechanism. Since $[V_B]$ and $[A_B]$ increase monotonically as composition changes from B to A,[14] it is most likely that the jumping of Cd is mediated by either $V_B$ or $A_B$ in these phases. Three mechanisms are consistent with the "abnormal" behavior in the early rare earth indides: the six jump cycle mechanism, the ring exchange mechanism, and the vacancy conversion mechanism.

(1) In the six jump cycle mechanism, a combination of defects is produced as the vacancy moves along the cycle. The defect combinations during a B-vacancy six jump cycle are shown below (recall Fig. 5):

| Start | 1st jump | 2nd jump | 3rd jump | 4th jump | 5th jump | 6th jump |
|---|---|---|---|---|---|---|
| $V_B$ | $V_A$ | $V_B$ | $V_A$ | $V_B$ | $V_A$ | $V_B$ |
| | $A_B$ | $A_B$ | $2\,A_B$ | $A_B$ | $A_B$ | |
| | | $B_A$ | $B_A$ | $B_A$ | | |

Similarly, the defect combinations during an A-vacancy six jump cycle are:

| Start | 1st jump | 2nd jump | 3rd jump | 4th jump | 5th jump | 6th jump |
|---|---|---|---|---|---|---|
| $V_A$ | $V_B$ | $V_A$ | $V_B$ | $V_A$ | $V_B$ | $V_A$ |
| | $B_A$ | $B_A$ | $2\,B_A$ | $B_A$ | $B_A$ | |
| | | $A_B$ | $A_B$ | $A_B$ | | |

We assume that the defect type that causes the highest free energy increase is $B_A$, since in rare earth indide systems B-atoms are much larger than A-atoms. As can be seen from the tables above, only one $B_A$ is produced during the six jump cycle starting with a B-vacancy, while two $B_A$s are needed during the cycle starting with an A-vacancy. Therefore one can expect the former cycle to have much lower free energy barrier and to be the dominating six jump cycle. If the B-vacancy six jump cycle is the primary operational jump mechanism, the jump frequency will be proportional to [$V_B$]. B-vacancy is a structural defect at the phase boundary A but needs to be thermally activated at the phase boundary B. Thus one has

$$Q_A = Q_6^m,$$
$$Q_B = Q_{V_B}^f + Q_6^m,$$

where $Q_{V_B}^f$ is the effective formation enthalpy of $V_B$ and $Q_6^m$ corresponds to the highest enthalpy barrier during a six jump cycle. The differences between the activation enthalpies for the two phase boundaries could therefore be attributed to the formation enthalpy of $V_B$.

(2) The ring diffusion mechanism does not require defects, however the presence of

certain types of defects may facilitate the exchange process. In Zener's analysis of ring diffusion in copper[13], the energy barrier for the ring exchange mainly arises from the (non-coulombic) repulsive interaction between positive ions, which could in principle be reduced by replacing large lattice ions with smaller ones or by taking them away. Since rare earth atoms are much larger than indium atoms, an antisite defect $A_B$ or vacancy $V_B$ could serve to reduce the energy barrier to ring exchange for the twelve A atoms surrounding it, which may form six 4-ring circles and/or eight 3-ring circles. Moreover, an $A_B$ itself could form twenty-four 3-ring circles with the surrounding A-atoms. If this is the principal jump mechanism, then Cd jump frequencies should be proportional to $[V_B]$ or $[A_B]$. Like in the six jump cycle mechanism, $[V_B]$ and $[A_B]$ are abundant as structural defects at the boundary A but need thermal activation at the boundary B, and one has

$$Q_A = Q^m_{ring},$$
$$Q_B = Q^f_{V_B} (\text{or } Q^f_{A_B}) + Q^m_{ring},$$

where $Q^m_{ring}$ corresponds to the maximal enthalpy increase during a ring rotation. And the differences between the activation enthalpies for the two phase boundaries could be attributed to the formation enthalpy of either $V_B$ or $A_B$.

(3) The vacancy conversion reaction $V_B + A_A \rightarrow A_B + V_A$ allows B-vacancies to be turned into A-vacancies. Even if only a small fraction of B-vacancies are converted, the so produced A-vacancies may still greatly outnumber thermal A-vacancies at not too high a temperature at the phase boundary A, where B-vacancies are abundant as structural defects. One then has

$$Q_A = Q^{tr} + Q^m_{V_A},$$

in which $Q^{tr}$ is the transfer enthalpy required for the conversion reaction and $Q^{m}_{V_A}$ is the migration enthalpy of A-vacancies. At the phase boundary B, A-vacancies still have to be thermally activated and one has

$$Q_B = Q^{f}_{V_A} + Q^{m}_{V_A}.$$

Therefore for this mechanism the differences between $Q_B$ and $Q_A$ could be attributed to $Q^{f}_{V_A} - Q^{tr}$.

All the three mechanisms discussed above would lead to jump frequencies higher at A boundaries than at B boundaries. However one more condition must be met in order for these mechanisms to be functioning: that $V_B$ or $A_B$ must jump at a frequency comparable to that of Cd. Otherwise part of the Cd probes that are in the vicinity of $V_B$ or $A_B$ will jump at a high frequency, while the probes that are away from defects will hardly jump at all. This would lead to two-signal spectra or significant inhomogeneous broadening of the spectra, which was not observed in the experiments. The migration of $V_B$ is included in the six jump mechanism. But in the other two mechanisms, the movement of $A_B$ or $V_B$ would be difficult as it requires jump distance longer than the nearest neighbor distance for defects on the A-sites to migrate. Based on this consideration, the B-vacancy six jump cycle mechanism is most likely to be the operational mechanism for Cd diffusion in the three early rare earth indides. Calculated values of $Q_B$ - $Q_A$ and interpretations according to the analysis above are given in Table 2.

Table 2. Differences between activation enthalpies at opposing phase boundaries

| Phases | $Q_B$ - $Q_A$ [eV] | Jump mechanism | Interpretations |
|---|---|---|---|
| $LaIn_3$ | 0.28(1) | B-vacancy six jump cycle mechanism | Differences between $Q_B$ and $Q_A$ are approximate formation enthalpies of $V_R$ |
| $CeIn_3$ | 0.39(8) | | |
| $PrIn_3$ | 0.58(9) | | |
| $NdIn_3$ | -0.1(1) | A-monovacancy mechanism | $Q_B$ and $Q_A$ are close because $V_A$ is thermally activated at both boundaries |
| $TmIn_3$ | -0.2(2) | | |
| $LaSn_3$ | -0.0(1) | | |

Moreover, Fig. 21 suggests that $Q_6^m$ increases as the lattice parameter decreases from $LaIn_3$ to $PrIn_3$. After about $NdIn_3$, $Q_6^m$ becomes larger than $Q_{V_A}^m$ and the A-monovacancy mechanism becomes the dominant jump mechanism. The measurements on $NdIn_3$ (A and B), $GdIn_3$ (B), $ErIn_3$ (B) and $TmIn_3$ (A and B) suggest that the activation enthalpies in the late rare earth indides depend on the lattice parameters to a much less degree.

# 6. Summary

Cd jump frequencies were measured in $L1_2$ type rare earth indides, gallides and aluminides, and compared with previous measurements on indides and aluminides. They were found to span a large range from ~6000 MHz in $LaIn_3$ (A) to less than 1 MHz in $ScAl_3$ at 1200 K. Activation enthalpies were fitted using the Arrhenius temperature dependence and were in the range 0.5 – 1.8 MeV, which are low compared with other metallic systems.

Measurements in rare earth indides were made at the opposing phase boundaries A and B, which were decided to have compositions that were significantly A-rich or very close to stoichiometry, respectively, using the free energy curves. A reversal in composition dependence was seen between the early and late rare earth indides, crossing over at about $NdIn_3$. $GdIn_3$, $TmIn_3$ and $LaSn_3$ have higher jump frequencies at the less A-rich boundary, which is in agreement with the widely accepted A-vacancy diffusion mechanism.

$LaIn_3$, $CeIn_3$ and $PrIn_3$ have lower activation enthalpies at the more A-rich boundary, which necessitates a more complicated diffusion mechanism. Three mechanisms were considered to explain the observed behavior, namely the B-vacancy six jump mechanism, the ring exchange mechanism and the vacancy conversion mechanism. These mechanisms lead to jump frequencies that are proportional to either $[V_B]$ or $[A_B]$, which increase monotonically with In mole fraction. The B-vacancy six jump cycle mechanism was decided to be the most likely mechanism as a result of the homogeneity of the spectra. Based on this mechanism, the differences in activation enthalpies at the

two phase boundaries, namely 0.28(1) eV for $LaIn_3$, 0.39(8) eV for $CeIn_3$, and 0.58(9) eV for $PrIn_3$ were attributed to formation enthalpies of rare earth vacancies.

# References


[1] M.O. Zacate, A. Favrot and G.S. Collins, Phys. Rev. Lett. 92 (2004), 225901

[2] G.S. Collins, A. Favrot, L. Kang, D. Solodovnikov and M.O. Zacate, Defect and Diffusion Forum 237-240, 195-200 (2005)

[3] H. Mehrer, Mater. Trans. JIM, 37, 1259 (1996)

[4] G.S. Collins, A. Favrot, L. Kang, E. Niewenhuis, D. Solodovnikov, J. Wang, and M.O. Zacate, Hyperfine Interact. 159, 1, (2004)

[5] Th. Wichert and E. Recknagel in *Microscopic Methods in Metals*, U. Gonser (Ed.), Springer-Verlag Berlin Heidelberg (1986)

[6] G. Schatz and A. Weidinger, *Nuclear Condensed Matter Physics*, J. Gardner (Ed.), Johns Wiley & Sons (1996)

7 H. Winkler and E. Gerdau, Z. Physik 262, 363 (1973)

8 W. Evenson, J. Gardner, R. Wang, H.-T. Su, and A. McKale, Hyp. Int. 62, 283 (1990)

9 A. Baudry and P. Boyer, Hyp. Int. 35, 803 (1987)

[10] H. Mehrer, *Diffusion in Solids*, Springer-Verlag Berlin Heidelberg (2007)

[11] T. Ito, S. Ishioka and M. Koiwa, Philos. Mag. A 62, 499 (1990)

[12] M. Koiwa, H. Numakura and S. Ishioka, Defect Diffus. Forum 143-147, 209 (1997)

[13] C. Zener, Acta Cryst 3, 346 (1950)

[14] G.S. Collins and M.O. Zacate, Hyperfine Interact. 136/137, 641 (2004)

[15] E. Nieuwenhuis, Technical report, *Lattice locations and diffusion of $^{111}$In/Cd atoms in $Ga_7Pd_3$* (2004)

[16] S.L.Shropshire, *Studies of point defects and defect interactions in metals using*

*perturbed gamma-gamma angular correlations,* Ph.D. dissertation, Washington State University (1991)

[17] G.S. Collins, *PAC data reduction at WSU*, lecture notes (2006)

[18] *Binary Alloy Phase Diagrams*, 2[ed] edition, T.B. Massalski (Ed.), ASM International (1990)

[19] R. Vianden, Hyp. Int. 15/16, 1080 (1983)

[20] G.S. Collins, J. Mater. Sci., 42, 1915 (2007)

[21] M. Forker and P. de la Presa, Phys. Rev. B, 76 115111 (2007)

[22] J.B. Adams, S.M. Foiles and W.G. Wolfer, J. Mater. Res., 4, 1, 102 (1989)

[23] P. Villars and L.D. Calvert, *Pearson's handbook of crystallographic data for intermetallic phases* (1985)